Cu^{2+}–Mn^{2+}-Co-doped CdO nanocrystallites: comprehensive research on phase, morphology and optoelectronic properties

Chitra Bhukkal[1] · Rachna Ahlawat[1]

Abstract

In this study, firstly cadmium hydroxide nanopowder was evolved by cost-effective wet chemical co-precipitation method. The transformation of nanocrystalline Cu^{2+}–Mn^{2+}-co-doped CdO occurred via thermal decomposition of the obtained hydroxide at 750 °C. The structural, optical and electrical behavior of nanocrystallites was analyzed by different complementary measuring tools. DTA of the as-prepared sample exhibited an endothermic peak at 240 °C attributed to crystallization. XRD analysis depicted a multiphase structure in the as-prepared sample, and pure rocksalt structure was obtained after annealing. Cu^{2+}–Mn^{2+}-co-doped cubic CdO has been achieved first time which was further confirmed by FTIR with various stretching and bending vibrations of Cd–O at 720, 625 and 460 cm^{-1}. SEM–TEM images demonstrated the brain-like morphology of different hexagonal and spherical nanocrystallites with an average size of ~ 35 nm. In addition, optical band gap energy was found in the range 2.14–2.44 eV by Tauc's plot. In photoluminescence results, emission spectra have many bands at 420, 480, 550 nm originated from excitonic transition, structural defects and oxygen vacancies, while intense peak at 450, 520 nm may be ascribed to Cu^{2+} and Mn^{2+} dopants, respectively. Hall measurements demonstrated that the Cu^{2+}–Mn^{2+}-co-doped CdO with a pure cubic phase has superior semiconducting behavior. The homogeneous codoping of Cu^{2+}–Mn^{2+} leads to efficient modification in structural, optical and electrical parameters of CdO which would make such materials attractive for semiconductor and photovoltaic industry, etc.

Keywords Cu^{2+}–Mn^{2+}-co-doped CdO · Multiphase structure · Absorbance · Photoluminescence · Resistivity · Mobility

✉ Rachna Ahlawat
rachnaahlawat2003@yahoo.com

1 Department of Physics, Material Science Lab, Chaudhary Devi Lal University, Sirsa, Haryana 125055, India

Introduction

Cadmium oxide (CdO) is a binary oxide belonging to the II–VI series of semi-conductors that has a direct band gap (~ 2.42 eV) and strong excitonic binding energy at room temperature [1]. The nanostructured CdO has been success-fully prepared in various morphologies just like nanobelts, nanotubes, nanorods, nanofibers, nanoscales, etc. [2]. Due to its direct band gap, it has many poten-tial applications in solar cells as optical windows, piezoelectronic, optoelec-tronic devices, field-effect transistor (FET) and in light-emitting diode [3, 4]. The presence of defects like oxygen vacancies and cadmium interstitials leads to the n-type character of pure CdO having conductivity of (10^2–10^4 S/cm). In the lit-erature, the n-type character of the semiconductor with low resistivity has been fulfilled by the doping of either single or double transition metals [5, 6]. Doping is the best suited procedure to manage the substantial character which specifi-cally controlled the band gap and electronic properties of semiconductors. There-fore, specific researches have been focused on the investigation of metal-doped nanocrystallites.

Many researchers have studied the optoelectronic properties of doped cadmium oxide with single metallic ions, e.g., tin (Sn), aluminum (Al), barium (Ba) and manganese (Mn) are few of them [7–10]. Sufficient reports of codoping in CdO have also been mentioned in the literature. In this regard, Gajbhiya et al. [11] have prepared the Li^{3+} and Eu^{3+}-co-doped CdO nanowires in an organic solvent by urea hydrolysis at a low temperature of 150 °C and their luminescence proper-ties were studied. They have observed that red emission significantly enhanced for co-doped CdO as compared to Eu^{3+}-doped CdO. Aydin et al. [12] outlined the effect of Zn doping (Zn + Li), (Zn + Na) and (Zn + K) double-doped nano-structured CdO films on the structural morphological and optical properties of the films. Gupta et al. [13] fabricated Li–Ni-doped CdO thin films using a sol–gel spin coating technique. The obtained results indicate that the nanostructure and optical band gap of the CdO films can be controlled by codoping. Bououdina et al. [14] prepared Cu^{2+} and Gd^{2+} ions-co-doped CdO by simultaneous thermal decomposition of precursors to prepare powder having room temperature ferro-magnetic properties which were tailored using doping. Kaya et al. [15] prepared Mn^{2+} and Mn^{2+}–Al^{3+}-doped CdO sample by sol–gel method and obtained cubic crystalline structure often annealing. They have mentioned that the optical band gap of CdO is lowered for Mn doped, while it is increased for the by Al-doped samples. Dakhel et al. [16] were systematically investigated the structure, optical and magnetic properties of the CdO nanocrystals co-doped with Al/Co, a redshift of the band gap results from that doping. It is investigated that codoping of tran-sition metals is influenced by the optical and electric properties significantly by tailoring energy level/surface states present in the host.

The optoelectronic behavior is generally modified by the position and coordi-nation of dopant ion into the lattice, and hence, the description of co-doped CdO is a prominent subject of the present investigations. Surprisingly, the luminescent property of co-doped CdO has not been addressed in many studies compared to

ZnS/CdS, although CdO is highly secured in contrast to sulfide because CdS oxidizes in the air [17, 18]. Keeping this in view, transition metals such as Cu^{2+} and Mn^{2+} have been recognized as the efficient dopants for CdO in this study and comprehensive research has been presented first time to explore the structural, optical and electrical behavior of the prepared samples. It is to be noticed that the impact of Cu^{2+}–Mn^{2+} combination modified the hylic character of CdO nanocrystallites that is directed by a few researchers only. Jawad et al. [19] prepared Mn-, Cu- and (Mn–Cu)-co-doped ZnS nanoparticles using the hydrothermal method at 180 °C. They have reported the effect of codoping in luminescence spectra where emission peaks showed a shift to longer wavelength. Ummartyatin et al. [20] successfully prepared Mn–Cu-doped ZnS by the wet chemical synthetic route. The understanding of substituted metal ions into ZnS leads to transfer the luminescent center by a little amount of dopants. In this study, when Cu^{2+} and Mn^{2+} ions are doped in CdO, the nanomaterials built a new area application in nanoscience like optical filters, microelectronic devices and in temperature gas sensor.

From the literature [11–20], it is suggested that a particular nanostructure is significantly influenced not only by the doping but also via proper thermal treatment. In the case of metal oxides, thermal treatment is implemented to trigger dopants. Throughout the process of annealing, not only optoelectronic properties changed, but materials structure and stoichiometry also changed. The imperfections and lattice defects will propagate in the entire structure of nanomaterials, and modification will occur at the high energy surface [18]. For comprehensive investigation on thermal, structural morphology and optoelectronic properties, the optimized annealing scheme has been implemented on Cu^{2+}–Mn^{2+}-co-doped CdO nanocrystallites.

Experimental details

Synthesis method

From the literature survey, it has been found that Cu^{2+}–Mn^{2+}-co-doped CdO prepared by several synthesis methods, i.e., 'spray pyrolysis,' 'molecular beam epitaxy,' 'vacuum deposition,' 'chemical bath deposition,' 'solution growth,' 'chemical vapor deposition,' etc. [16–20]. The above mentioned synthesis methods have utilized spatial confinement using various surfactants/capping agents in the doped CdO nanoparticles. The surfactants/capping agents exist simultaneously in the host matrix and act as a trap for nanoparticles. Among the various fabrication techniques, the wet chemical co-precipitate method is defined as the most suitable method for the fabrication of metal oxides in which chances of contamination from outside are negligible. During the synthesis of binary or ternary oxide system, the major issue is to manage the homogeneity and contamination due to difference in the relativity of different metals. Co-precipitation is a famous chemical route for the controlled particle size, excellent purity and uniform production of powder samples [21]. The names of the prepared samples, their annealing conditions and the corresponding designation used in the presented study are mentioned in Fig. 1.
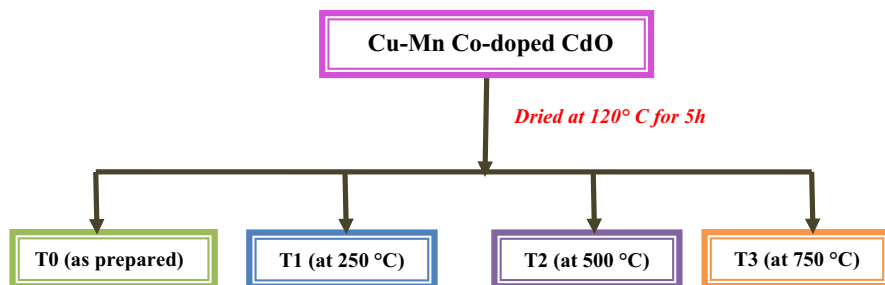
Fig. 1 Flowchart for designation of Cu^{2+}–Mn^{2+}-co-doped CdO nanocrystallites

We have purchased 0.2 M cadmium acetate hydrate [Cd(CH₃COO)₂ 2H₂O] and 0.05 M sodium hydroxide (NaOH) purchased from Sigma Aldrich with purity ≥ 99.99%. Also, 0.005 M copper acetate tetrahydrate [(C₄H₆CuO₄)4H₂O] and 0.005 M manganese acetate tetrahydrate [(C₄H₆MnO₄)4H₂O] with ≥ 98% purity were used as dopants. A successful synthesis of Cu^{2+}–Mn^{2+}-co-doped CdO nanocrystallites has been achieved by the cost-effective and easy co-precipitation method. The complete description of the sample preparation is mentioned in our earlier publication [22].

Characterization tools

In the present research work, Cu^{2+}–Mn^{2+}-co-doped CdO samples were characterized by well-known measuring tools. The X-ray diffraction (XRD) of prepared nanopowder has been observed by XPERT-PRO x-ray diffractometer, operated at 50 kV and 45 mA. The particular X-rays were emitted from Cu Kα radiation of wavelength 1.5406 Å in the interval of 2° angle. The elemental composition of respective samples was analyzed by X-ray energy-dispersive spectroscopy (EDS). The nanocrystalline size and surface modification of the annealed samples were examined by SEM and TEM. Fourier transform infrared (FTIR) spectra of the prepared nanostructures were analyzed PerkinElmer 400 spectrophotometer in the 450–4000 cm^{-1} range. The surface texture of the prepared nanopowder was investigated by FESEM (FEI Nova NanoSEM-450) with an accelerating voltage of 25 kV in coexistence with EDS (Bruker XFlash® 6|30) apparatus. UV–Vis spectra were analyzed using Lambda 750 (PerkinElmer) UV–Vis–NIR spectrophotometer in the specific range of wavelength 200–900 nm. The luminescence of the samples was examined using the PerkinElmer fluorescence spectrometer (model LS-55). The electrical parameters were examined according to the standard Van der Pauw configuration of Hall measurements at room temperature (0.5 Tesla magnetic fields). For this, pellets were developed in the form of a disk having diameter 20 mm and thickness of 250 nm.

Results and Interpretation

Thermal Study

TG and TDA graphic curves of as-prepared Cu^{2+}–Mn^{2+}-co-doped CdO are shown in Fig. 2a, b. The thermo-gravimetric graph depicted the ~30% overall weight loss in the temperature range 25–800 °C due to the decomposition and modification of precursors in different phases. One may notice that the total weight loss has occurred in five steps at different temperatures. Each step executed a unique decomposition which leads to a specific type of reaction between the precursors. Beyond 780 °C, there is a negligible weight loss; this means crystallization has been completely up
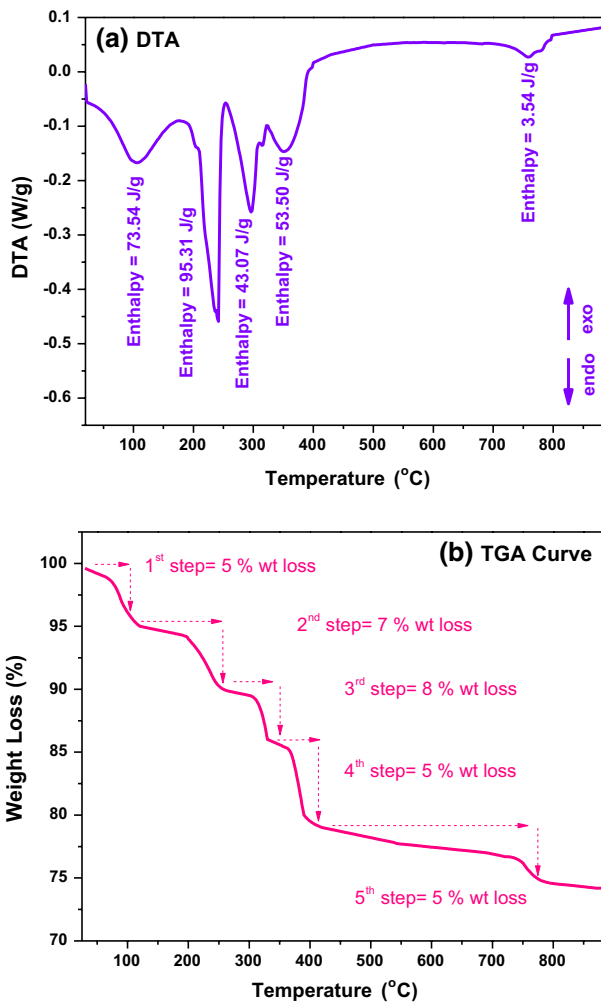

Fig. 2 **a** DTA curve, **b** TGA graph for as-prepared Cu^{2+}–Mn^{2+}-co-doped CdO nanocrystallite (T0)

to this temperature. In thermal differential curve of as-prepared sample, an endothermic peak is appeared at 100 °C due to the removal of water and acetates. The most prominent endothermic peak occurred at 240 °C is attributed to the crystallization process lead to a hexagonal phase with 7% weight loss [23]. Two other small peaks are found at 300 and 350 °C generated from the combustion of residual alkoxy groups and acetates within the precursors. These peaks correspond to the 3rd and 4th step with subsequent weight loss ~8 and 5% as shown in Fig. 2b. In addition, one most important change has been noticed at high temperature region where a broad peak is located around 750 °C with minimal weight loss ~5%. The latter is ascribed to complete phase transformation from hexagonal $Cd(OH)_2$ to cubic CdO which exists as the most prominent phase in annealed samples [22].

As shown in Fig. 2a, enthalpy corresponding to each peak is obtained by inbuilt software in the thermal analyzer. The main endothermic peak at 240 °C has enthalpy 95.31 J/g which insured that sample absorb heat at the particular temperature. The peak at 100 °C exists corresponding to the removal of volatiles has enthalpy 73.54 J/g. Further, two endothermic peaks appeared at 300 and 750 °C in the DTA curve have enthalpies 43.07 and 3.54 J/g, respectively, which warranted the conversion process from hexagonal $Cd(OH)_2$ to the cubic phase of CdO. At last, it is confirmed that the no mass decay was predicted beyond 750 °C, indicating the formation of finally Cu^{2+}–Mn^{2+}-co-doped CdO nanocrystallites with no impurity phase.

Crystallographic study

Interesting crystallographic information is obtained from the X-ray diffraction pattern of as-prepared and annealed samples when Cu^{2+}–Mn^{2+} co-doped in CdO powder as shown in Fig. 3a. In as-prepared sample T0, many small and intense diffraction peaks appear. The observed diffraction peaks in T0 sample are centered at $2\theta = 17.68°$, 23.57°, 30.20°, 35.13°, 36.22°, 39.85°, 43.49°, 47.72°, 49.71°, 52.25°, 57.86°, 61.43°, 65.17° and 74.90° corresponding to the mixed (hexagonal and monoclinic) phases of cadmium hydroxide. From these diffraction peaks, prominent peaks appeared at $2\theta = 23.57°$, 30.20°, 35.13°, 39.85°, 43.52°, 52.23°, 57.86°, 61.43° and 74.90° are affiliated to hexagonal cadmium hydroxide [25, 26]. These peaks could be attributed to the following miller indices (001), (100), (101), (002), (102), (110), (003), (200), (201) and (112), respectively. The lattice constant '*a*' (=0.3429 nm) and '*c*' (=0.4708 nm) are evaluated for hexagonal structure using standard equations that are matched with JCPDS card number 31-0228 [26]. Also, few small peaks appear at $2\theta \sim 17.68°$, 36.22°, 47.72° and 49.71° which possessed reflection planes (110), (220), (141) and (231), respectively. These diffraction peaks are associated with a monoclinic phase of $Cd(OH)_2$ as per JCPDS card no. 84-1767 [27].

For detailed study of developed phases in Cu^{2+}–Mn^{2+}-co-doped CdO, different annealing schemes are employed on prepared powder and obtained some amazing results. In sample T1 (annealed at 250 °C), the intensity of diffraction peaks corresponding to monoclinic and hexagonal $Cd(OH)_2$ are slightly increased as compared to sample T0. The highly intense diffraction peaks attributed to the sample T1
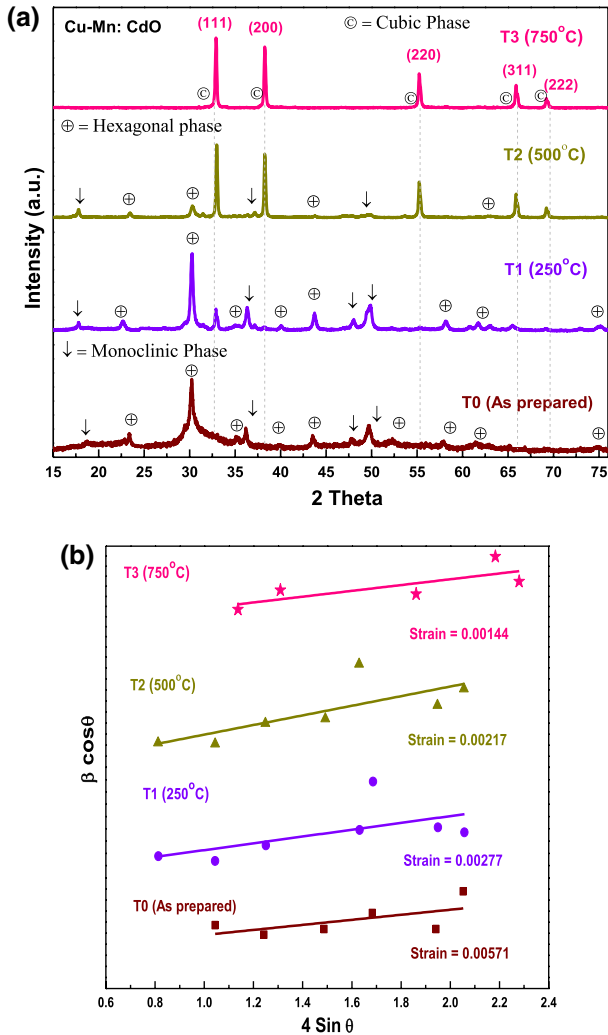
Fig. 3 **a** XRD pattern, **b** W–H plot for as-prepared and annealed samples of Cu^{2+}–Mn^{2+}-co-doped CdO nanocrystallites

established the creation of large nanocrystallites of Cu^{2+}–Mn^{2+}-co-doped $Cd(OH)_2$, while the width of diffraction peaks in the XRD spectra corroborates the crystalline nature of the prepared powder. One may notice a small peak also appears in this diffractogram at $2\theta \sim 32.90°$ which is well matched with (111) reflection plane of cubic phase of CdO [22]. On further annealing, in sample T2 (at 500 °C), the diffraction peaks corresponding to hexagonal and monoclinic phases are almost disappeared, while intensity of peaks attributed to cubic CdO is significantly enhanced.

Furthermore, in the highest annealed sample T3 (at 750 °C), a face-centered cubic structure of CdO is completely evolved which has space group $FM\overline{3}m$ {225}.

The corresponding peaks appear at $2\theta \sim 32.93°$, $38.34°$, $55.17°$, $65.78°$, $69.15°$ with (111), (200), (220), (311), (222) reflection planes as depicted in Fig. 3a. The appeared diffraction peaks, lattice parameter and the (hkl) values are well matched with the standard JCPDS: 05-0640 [28–30]. In this diffractogram, no other impurity peaks are found pointing that hexagonal $Cd(OH)_2$ phase is completely transformed in cubic CdO. Sharp peaks of the XRD pattern appeared in sample T3 indicated that the fabricated Cu^{2+}–Mn^{2+}-co-doped CdO powder is highly dense and possessed a good crystalline structure. The detail of all the diffraction peaks that appeared in sample T3 is given in Table 1 with corresponding intensities (%) and miller indices. For every reflection plane in most annealed sample (T3), 'd' spacing and lattice parameter 'a' are calculated and summarized in Table 1. It is to be noticed in all prepared samples that there is no explicit peak assigned to MnO or CuO phase implying that both dopants have successfully substituted Cd ion at the lattice site of CdO.

Crystalline size

The average crystalline size (D) is calculated for all samples by Debye–Scherrer's equation:

$$\text{Crystalline size} \left(\mathcal{D}_{D-S}\right) = \frac{0.94\lambda}{\beta_{hkl} Cos\theta_{hkl}}. \tag{1}$$

The wavelength of the radiation is given as 'λ' in the above equation, β_{hkl} is the full width at half maxima (FWHM), θ_{hkl} is the Bragg diffraction angle [26]. Here, crystallite size for Cu^{2+}–Mn^{2+}-co-doped CdO is found to be 16, 28, 32 and 36 nm, respectively, for T0, T1, T2 and T3 sample. It is observed that the crystalline size is increased with annealing temperature which is well in agreement with other studies [22].

Lattice strain

The variation in nanocrystalline size and different crystallographic structures probably related to the internal strain which is evaluated using the well-known W–H equation as given here in Eq. (2).

Table 1 Structural parameters for T3 sample of Cu^{2+}–Mn^{2+}-co-doped CdO nanocrystallites

Sr. nos.	2θ	hkl Plane	'd' $= \frac{\lambda}{2Sin\theta}$ in nm	'a' $= $'$d$' $\sqrt{h^2 + k^2 + l^2}$ in nm	Relative (I) intensity	(I') JCPDS: 05-0640	Texture para (χ)
1.	32.93	(111)	0.272	0.4717	100	100	1.0303
2.	38.34	(200)	0.234	0.4681	87	88	1.0186
3.	55.17	(220)	0.166	0.4695	42	43	1.0063
4.	65.78	(311)	0.141	0.4676	27	28	0.9934
5.	69.15	(222)	0.136	0.4711	12	13	0.9510

$$\frac{\beta \mathrm{Cos}\theta}{\lambda} = \frac{1}{\mathcal{D}} + \varepsilon\frac{4\mathrm{Sin}\theta}{\lambda} \tag{2}$$

where the strain factor is denoted by 'ε' and average crystallite size is represented by $\mathcal{D}$ in a direction orthogonal to the surface of the sample [33]. In this study, micro-strain is calculated by plotting a graph between $4 \sin \theta$ and $\beta \cos \theta$ for each sample and displayed in Fig. 3b. The strain present in the lattice is evaluated from linear fit of the line obtained as 5.71×10^{-3}, 2.71×10^{-3}, 2.17×10^{-3}, 1.44×10^{-3} for all the prepared samples T0, T1, T2 and T3, respectively. These calculated values of strain are also mentioned in Table 3, and its variation with annealing temperature is further exhibited in Fig. 10b. It is suggested that lattice strain is significantly decreased due to annealing (and a pure and highly crystalline structure of CdO is derived at highest annealed temperature ~ 750 °C). It is pertinent to mention here that the estimated nanocrystallite size is comparatively larger than the size achieved by Debye–Scherer's formula (due to presence of microstrain). In Debye–Scherer's formula, the component of strain is expected to be zero and only reduced nanocrystallite size is accountable for the broadening in the diffraction peaks. As a result, slight increase in the particle size is noticed.

Preferred Orientation (χ)

In the present study, we have obtained polycrystalline Cu²⁺–Mn²⁺-co-doped CdO with its main five planes (111), (200), (220), (311) and (222). The extent of preferred orientation (χ) of the synthesized samples has been obtained by the average value of all the specified texture parameter (Φ) for each (hkl) plane. We have calculated the extent of preferred orientation using the equation as follows:

$$\chi = \sqrt{\frac{\sum_{i=1}^{X}\left(\Phi_i - \Phi_{io}\right)^2}{X}}. \tag{3}$$

In the above relation, Φ_i is the mean of the calculated texture parameter and Φ_{i0} is the individual value for each diffraction plane (hkl) [22]. In general, when (i) we take $\chi = 0$, it implies random orientation and (ii) $\chi \neq 0$ confirms the improved preferred orientation of the synthesized powder along a particular crystallographic plane (hkl). Therefore, to analyze the extent of preferred orientation in a better way, firstly there is a need to define texture parameters. XRD diffractogram revealed the evaluation of texture parameter (Φ) for T3 sample with the help of the relation given below:

$$\Phi_{(hkl)} = X\frac{I_{(hkl)}/I'_{(hkl)}}{\sum_x I_{(hkl)}/I'_{(hkl)}}. \tag{4}$$

Here, the observed intensity of a plane (hkl) is represented as $I_{(hkl)}$, the actual intensity of the particular plane (hkl) is given as I'_{hkl} which is extracted from the JCPDS card no. (06-540), X is the total number of reflection plane which is taken five in this study and x is the number of diffraction peak [6, 34]. Using Eq. (4), we

have found the texture parameter (Φ) as 1.0303, 1.0186, 1.0063, 0.9935 and 0.9510, respectively, for each plane which is also given in Table 1. These results inferred that the growth mechanism of the prepared nanopowder has preferred orientation along (111) plane and in fair agreement with the literature [8–11]. Further, with the help of these texture parameters in Eq. (3), the numeric value of extent of preferred orientation (χ) has been obtained ~0.89. The non-vanishing value of 'χ' emphasized that Cu^{2+}–Mn^{2+}-co-doped CdO nanocrystallites have preferred orientation along (111) crystallographic plane. In the present study, (111) is preferred as the most stable growth direction instead of [100] of hexagonal $Cd(OH)_2$ dominated in samples T0 and T1.

Vibrational study

Vibrational characteristic modes of KBr dispersed as-prepared and annealed samples T0, T1, T2 and T3 are depicted by Fourier transform infrared spectroscopy as illustrated in Fig. 4. The infrared spectroscopy is mainly important for a better understanding of different vibrational modes of Cd–O/Cd–OH during the formation of Cu-Mn-co-doped CdO. The phase confirmation and functional group analysis of the materials related to the multi-component system is performed by FTIR technique. Figure 4 shows the FTIR spectra of Cu–Mn-co-doped CdO nanopowder with heat treatment at 250 °C, 500 °C and 750 °C for 2 h. The appeared small and broad peaks are attributed to vibrations of different organic/inorganic groups and their overtones.

In FTIR spectra, the range of 3600–3200 cm^{-1} shows a broadband attributed to the stretching of O–H in water molecules. The specific broad transmittance due to vibrations of the hydroxyl group occurred at 3598, 3596, 3594 and 3592 cm^{-1}, respectively, for T0, T1, T2 and T3 samples. These peaks have coercively corroborated the impendence of hydroxyl ions during the fabrication of the samples [28–30]. The details of present molecules, their groups and the corresponding vibrations are tabulated in Table 2. Small peaks lie at 2358, 2356, 2354 and 2350 cm^{-1} are attributed to CO_2 vibrations, absorbed by all samples from the environment [31]. With annealing temperature, the area of H_2O and CO_2 peaks is reduced, and in the highest annealed sample (T3), these impurity peaks are almost disappeared. Symmetric vibrations of acetate complex COO^- present in the precursors are observed at 1418, 1416, 1412 and 1410 cm^{-1} for all prepared samples [33] as given in Table 2.

In sample T0, the peaks at 1032 and 930 cm^{-1} are attributed to the stretching and bending vibrations of the C–H and residual organic complexes [32]. The bending vibrations of C–H bond are shifted at 1115, 1113 and 1110 cm^{-1} in T1, T2 and T3 samples, respectively [32]. The IR absorbance lies in the region 650–640 cm^{-1} and 730–720 cm^{-1} that are attributed to symmetric and asymmetric stretching vibrations of Cd–O [21]. In addition, the characteristic bending vibrations of the metal–oxygen bond are highlighted at 464, 462, 460 and 458 cm^{-1} for T0, T1, T2 and T3 sample, respectively [30–34]. This outcome of FTIR spectra demonstrates that the Cu^{2+}–Mn^{2+} is significantly doped and the transformation of $Cd(OH)_2$ into CdO takes place efficiently due to annealing [20]. The acquired FTIR results are in a valid compromise with the XRD explication and TG–DTA findings.
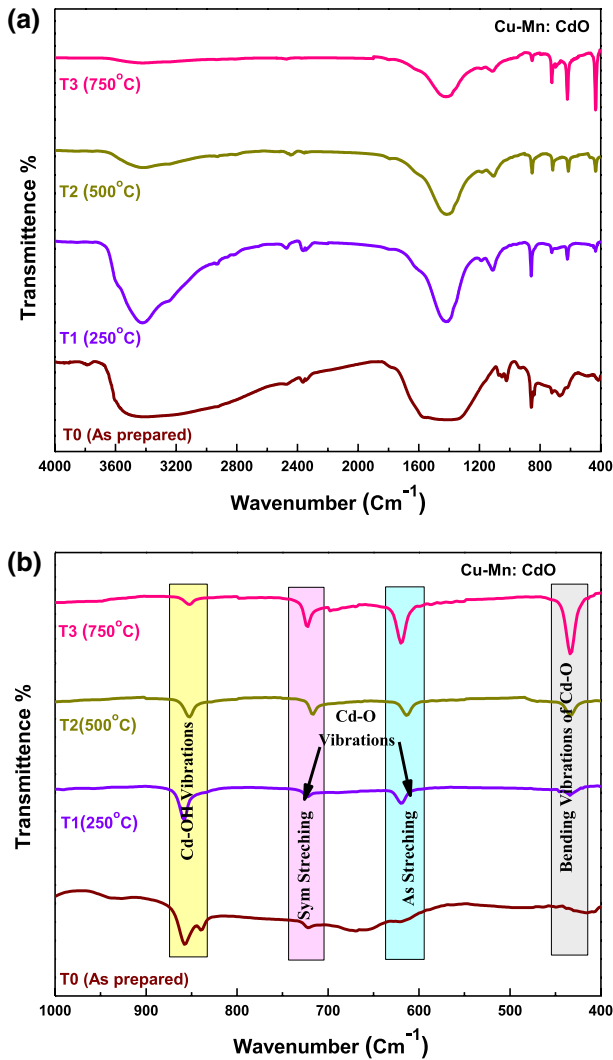
Fig. 4 FTIR spectra of as-prepared and annealed samples of Cu²⁺–Mn²⁺-co-doped CdO nanocrystallites

Surface and EDS study

The surface morphology of as-prepared Cu²⁺–Mn²⁺-co-doped CdO and annealed samples (T1, T2 and T3) is examined by SEM, and their compositional verification is done by EDS. A clear signal and dilation of Cu²⁺–Mn²⁺-co-doped CdO nanocrystallites synthesized at various annealing temperatures are shown in Fig. 5. The nanocrystallites in the T0 sample are not only hexagonal but some elliptical, square, spherical shapes are well marked. In the T1 sample, as the annealing temperature is implemented (~250 °C), the densification of the sample is increased and the space

Table 2 FTIR peaks assignment of as-prepared and annealed samples of Cu^{2+}–Mn^{2+}-co-doped CdO nanocrystallites

Sr. nos.	Wave number (cm^{-1})				Group assignment for wave numbers
	T0	T1	T2	T3	
1.	3598	3596	3594	3592	Stretching vibration of the absorbed water molecules (H_2O)
2.	2358	2356	2354	2350	O=C=O vibration absorbed from environment.
3.	1418	1416	1412	1410	Symmetric vibration of acetate complex (COO^-)
4.	1032	1115	1113	1110	Attributed to bending of C–H bond
5.	862	860	856	852	Corresponding to Cd–OH vibrational modes
6.	728	724	720	722	Attributed to symmetric stretching vibrations of Cd–O
7.	628	626	624	620	Due to asymmetric stretching of Cd–O bond
8.	464	462	460	458	Because of Cd–O (metal–oxygen) bending vibrations

between different grain boundaries is reduced. The SEM images at 500 °C and 750 °C revealed that particles are agglomerated to some extent and almost have a spherical shape. This result shows a good deal between FTIR and XRD analysis.

Figure 5 exhibits that FESEM images are composed of densely packed brain shape nanostructures which have great importance and potential applications in various fields due to their high specific surface area [35]. Major chemical and elemental compositions like Cd, O, Cu^{2+}, Mn^{2+} in the synthesized nanopowder are displayed in EDS spectra (Fig. 5). The quantities of Cu^{2+} and Mn^{2+} estimated by EDS are good agreement with actual concentration of Cu^{2+} and Mn^{2+} doping in the prepared nanopowder. These observations depicted the successful doping of Cu^{2+}–Mn^{2+} at the site of cadmium ion in CdO lattice.

TEM analysis

The TEM technique analyzed the size and morphology of the Cu^{2+}–Mn^{2+}-co-doped CdO nanopowder. Figure 6 represents the micrographs for the thermally treated samples T0, T1, T2 and T3. In as-prepared T0 sample, various elliptical, nearly spherical and quasi-spherical nanostructures indicating crystalline nature of cadmium oxide and little cores grains emphasized the presence of hexagonal structure of cadmium hydroxides. It is quite evident from the TEM micrograph of the T1 sample that the contents of surface water, Cd–OH and volatile matter decreased and as a result the density of the sample increased. Moreover, the replacement of few white patches by dark patches in the micrograph suggests the development of the both hexagonal and monoclinic phases of $Cd(OH)_2$ which is fairly supported by XRD and FTIR data of the corresponding sample. When the sample is annealed at 500 °C, a significant change in the grain size and surface morphology is noticed. TEM image (T2) emphasized improvement in the spherical shape and nano disparity of the cadmium oxide nanocrystallites. This micrograph also exhibits that Cu^{2+}–Mn^{2+}-co-doped CdO is made up of non-agglomerated spherical shape particles. Further at 750 °C (sample T3), mostly crossed link spherical structures are observed in the
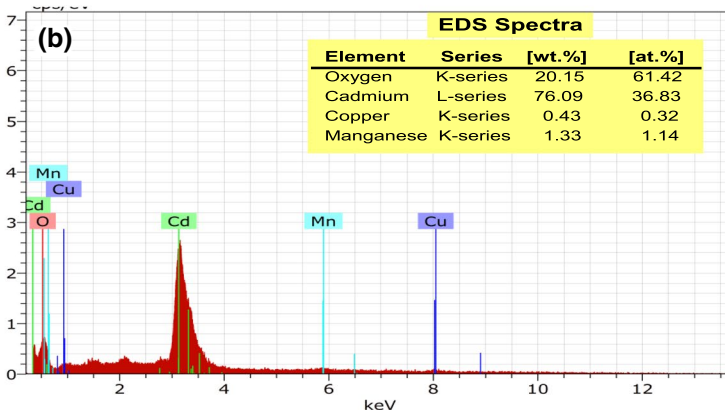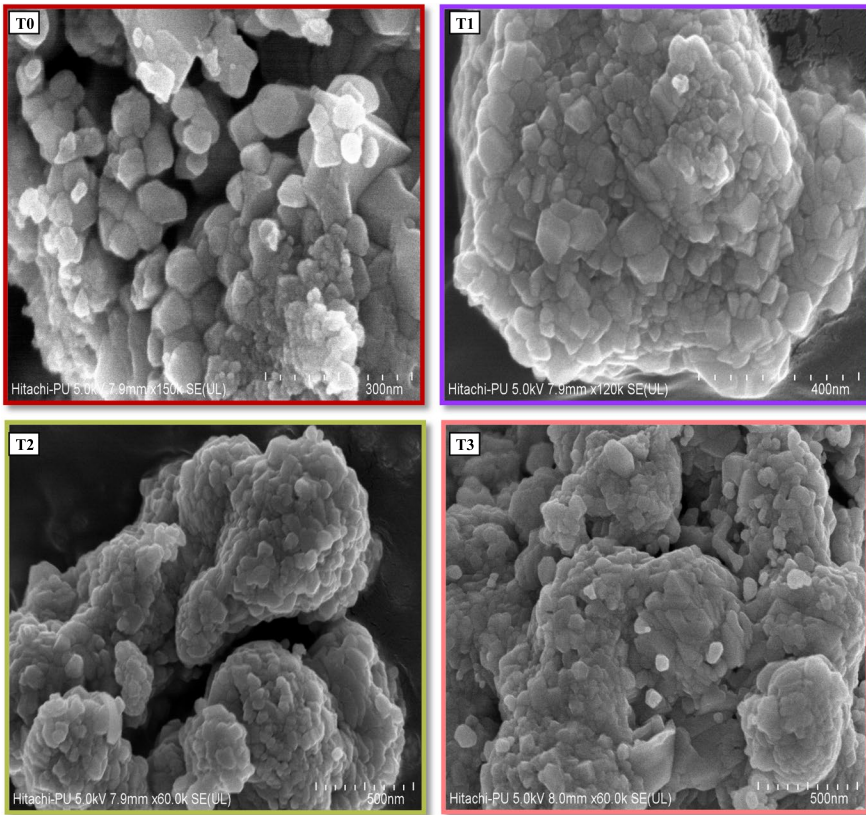
(a)

(b)

Fig. 5 **a** SEM images of as-prepared and annealed samples, **b** EDS spectra of as-prepared Cu^{2+}–Mn^{2+}-co-doped CdO nanocrystallites (T0)
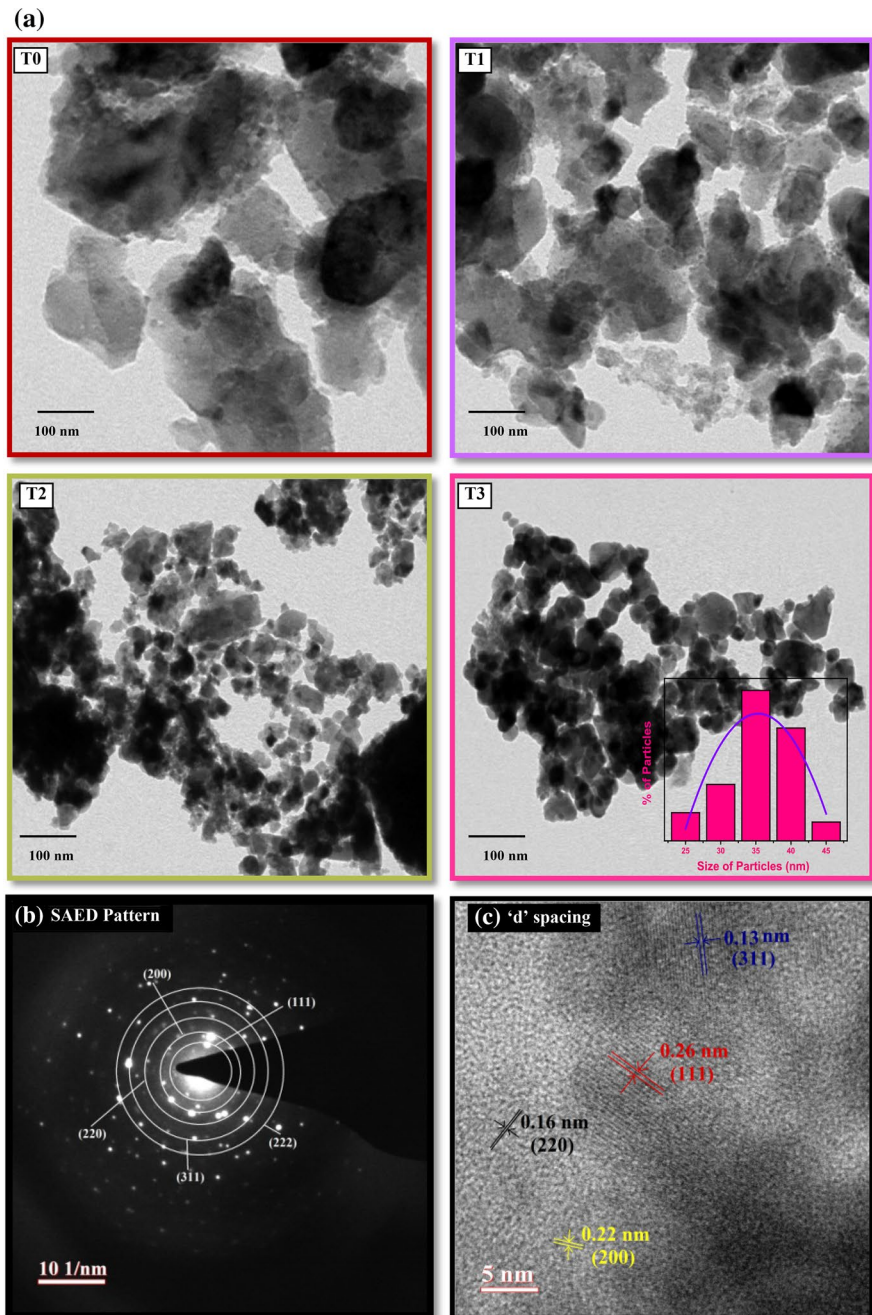
Fig. 6 a TEM images of as-prepared and annealed samples of Cu^{2+}–Mn^{2+}-co-doped CdO nanocrystallites, b SAED pattern, c HRTEM image of T3 sample

corresponding micrograph. Therefore, the pore and hydroxyl matter are reduced due to annealing, and consequently, hexagonal $Cd(OH)_2$ is deformed and leads to the development of a highly crystalline cubic CdO phase.

The selected area electron diffraction (SAED) pattern of Cu^{2+}–Mn^{2+}-co-doped cadmium oxide is shown in Fig. 6 which exhibits the well-developed polycrystalline structure of prepared powder. The miller indices of diffraction rings appeared in SAED pattern are matched with a cubic crystalline phase of CdO. In the present study, we have also calculated the average sizes of nanocrystallites by plotting the histogram for most annealed sample T3. Approximately 25 particles are selected randomly and plotted their percentile according to their size range [36]. The average diameter of nanocrystallites is investigated ~ 35 nm using histogram and TEM scale which is in good agreement with the value obtained from the Scherer's formula mentioned in XRD analysis. The HRTEM micrograph in Fig. 6 presented the different fringes oriented in different directions specified with the corresponding lattice parameter. The 'd' spacing for different oriented planes (111), (200), (220) and (311) is estimated approximately 0.26, 0.22, 0.16 and 0.13 nm, respectively. The SAED pattern, lattice fringes and histogram demonstrated that annealing is efficiently improved the densification and crystallinity of Cu^{2+}–Mn^{2+}-co-doped CdO samples which are in fair agreement with the XRD-FTIR and SEM–TEM findings.

Optical absorbance study

This technique is used to study the absorption ability of as-prepared and annealed samples of Cu^{2+}–Mn^{2+}-co-doped CdO powder during the growth of nanocrystallites. The wavelength of the light absorbed is the characteristic of its chemical structure. UV–visible absorption of light may result in the agitation of electrons in a system of nanomaterials from the ground state to excited states. Figure 7a shows the variation of optical absorption with incident photon wavelength in the range 200–800 nm for as-prepared (T0) and annealed samples (T1, T2 and T3) at room temperature.

A fixed weight percentage of each precursor of Cu^{2+} and Mn^{2+} is co-doped in CdO powder and then dispersed in ethanol by ultrasonic treatment and obtained considerable absorption in the ultraviolet region to visible region [24]. As shown in Fig. 7a, a broad absorption hump appears in the range 220–380 nm and the band edge lies in the visible region. UV–Vis spectra inferred that the absorption band maxima shifted from lower wavelength (room temperature) to higher wavelength (at 750 °C) with annealing, which signifies the formation of larger particles at higher temperature due to agglomeration. The prepared nanopowder exhibited almost negligible absorption in the optical range, hence can be used as window materials (TCOS) and waveguides.

Nanocrystallite size, imperfections at the grain boundaries and oxygen deficiency are the prime factors which abruptly influence the optical absorption [37]. In the present work, the absorption coefficient is slightly shifted toward higher wavelength region resulting in the formation of nanoparticle clustering due to applied thermal treatment. Such a redshift occurred in agglomerated samples encouraged the
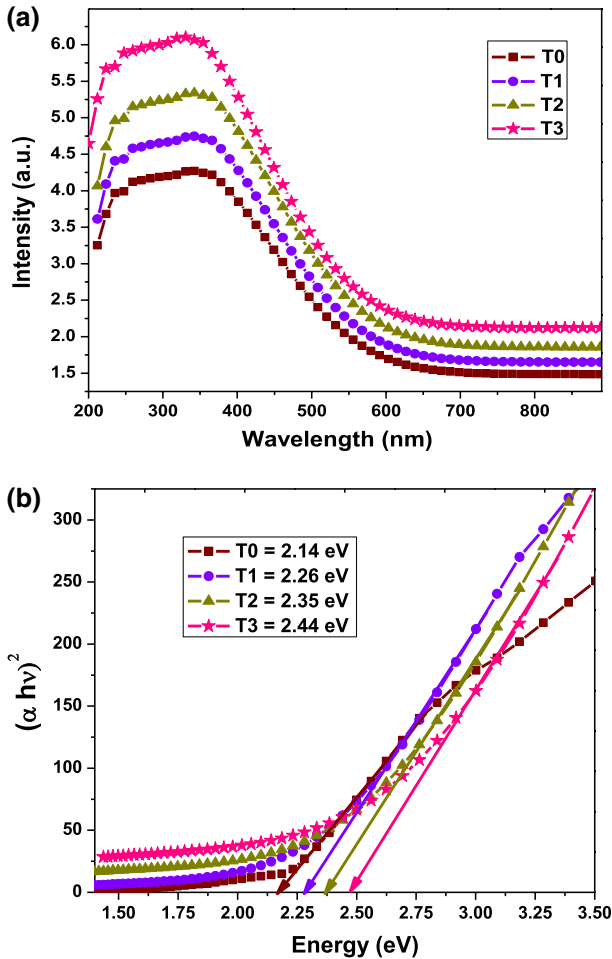
Fig. 7 a UV–visible absorption spectra, **b** band gap energy of as-prepared and annealed samples of Cu^{2+}–Mn^{2+}-co-doped CdO nanocrystallites

utilization of prepared nanopowder in modern solar cells and other heterojunction optoelectronic devices. The optical band gap E_g of the synthesized nanopowder is decided from the absorbance spectra, where a sharp enhancement in the absorption is considered from band to band transition.

The observed absorbance in all samples is dominant in the short wavelength region. It emphasized that direct allowed transition has the only possibility to occur at the same value of crystal momentum. Therefore, the optical absorption is being used to decide the fundamental nature and exact value of the band gap energy using the relation of absorbance and photon energy incident on the sample. In this way, the observed band gap energy (E_g) of the Cu^{2+}–Mn^{2+}-co-doped CdO nanocrystallites is estimated by the following equation:

$$(\alpha h\nu)^{1/m} = B(h\nu - E_g). \tag{5}$$

In the above relation, α is the observed absorption coefficient and the probability of the transition is defined by an integer 'm' [36]. Figure 7b displays the plot of $(\alpha h\nu)^2$ versus photon energy ($h\nu$) curve where a straight line portion at higher energy values (˃2.5) confirms the direct optical transition [25, 26]. The optical band gap is deliberated by extrapolating the straight portion of the graph at the energy axis ($x = 0$). The band gap energy (E_g) of as-prepared sample T0 is obtained as 2.14 eV which is smaller than the band gap energy of undoped CdO (2.54 eV). This redshift is noticed due to the presence of many energy levels assigned to different impurity phases. Also, E_g is calculated for annealed samples T1, T2 and T3 samples as 2.26, 2.35 and 2.44 eV, respectively. With annealing, a slight increase in band gap energy resulted from the removal of surface defects and the occurrence of phase transformation from $Cd(OH)_2$ to CdO [19, 23]. Due to codoping, there is an enhancement of free carriers in the C.B. which results in a shift in the Fermi level leading to an expansion of the optical band gap of degenerate semiconductor [17]. A blueshift has been noticed in the band gap of Cu^{2+}–Mn^{2+}-co-doped CdO could be ascribed to the Burstein–Moss (BM) effect [38]. The resulting strength of carrier concentration further helps to improve the electrical properties of prepared samples as discussed in the next section.

Emission spectra

From the results of XRD-FTIR, SEM–TEM and UV–Vis analysis, it is discovered that room temperature photoluminescence must be conducted for optical investigation as-prepared (T0) and annealed samples (T1, T2 and T3) of Cu^{2+}–Mn^{2+}-co-doped CdO nanocrystallites. In fact, the photon emission mechanism is directly associated with electronic structure and as a result transitions occurred in dopant and host materials [38]. The difference in the electronic behavior of bulk material with their nanoscaled counterpart is generated due to the change in the corresponding density of states [39]. In this regard, an excitation wavelength $\lambda_{ex} = 300$ nm from xenon lamp source has been used to perform the PL measurements of all the prepared samples at room temperature.

All the prepared samples show similar emission peaks positioned at 420, 450, 480, 520 and 550 as shown in Fig. 8. The peak at 420 nm is originated from excitonic transitions of the electrons present in the C.B. and the holes available in the V.B. Such violet emission is also attained for undoped CdO as represented in the literature [40]. The emission peak at 480 and 550 nm may be ascribed to deep trap state emission and structural defects such as oxygen vacancies on the surface that are less size dependent [41]. The origin of the most prominent peak observed 480 nm is not clearly understood. However, it may either belong to pure CdO or from luminescent centers created by Cu ions. The emissions from Cu ions were reported quite differently by different authors because of different quantum sizes, surface defects, impurity levels in the band gap, different hosts and different synthesis techniques [40–42]. A small, broad hump in the green
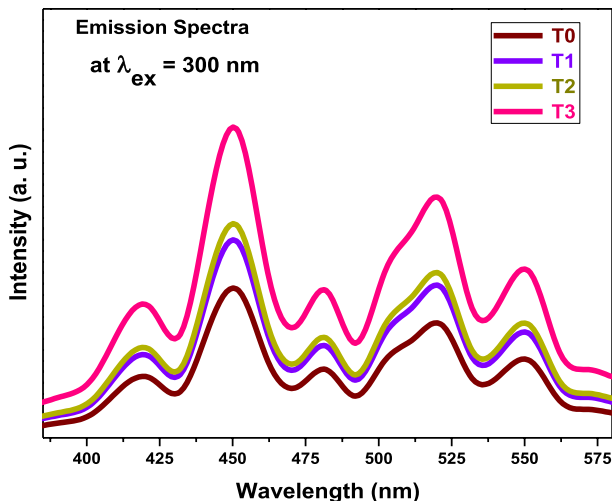
Fig. 8 Emission spectra of as-prepared and annealed samples of Cu^{2+}–Mn^{2+}-co-doped CdO nanocrystallites

region of the electromagnetic spectrum is centered at 520 nm corresponding to the $^4T_1$–$^6A_1$ transition of manganese ions (Mn) which can easily form recombination centers near-band-edge [19]. It is worth mentioning that the position of the emission bands is not changed when temperature is raised from 250 to 750 °C. One may notice that intensity in annealed samples is increased linearly with the temperature and attains almost twice value in the highest annealed sample T3 in comparison with as-prepared sample T0 [22–24]. The obtained results are well in agreement with the literature where Kripal et al. [42] have prepared Mn-doped II–VI semiconductor and they obtained similar emission peaks at 417, 446, 480 and 520.

Energy level diagram

Generally, in the luminescent mechanism, the doped ions (Cu^{2+}, Mn^{2+}) set up deep trap energy levels between V.B. and C.B. of CdO. By absorbing the excitation energy, free carriers are jumped from V.B. to C.B. and relaxed at shallow defect states generated by Cu^{2+} and Mn^{2+} ions. Then, the excited carriers (e^-) are coupled with holes left in the conduction band. Also, holes migrated to dopant ion energy states by radiative transitions, which produce photon emission. Therefore, it became possible to observe emission from CdO and Cu^{2+} and Mn^{2+} clusters at the same time. In the present study, because oxygen ions have larger ionic radii (1.4 Å) than that of cadmium ions (0.94 Å), interstitial oxygen produced more strain in the CdO and thus leads to significant emission in the visible region. A schematic diagram of various radiative transitions that lead to enhanced emission is exhibited in Fig. 9.
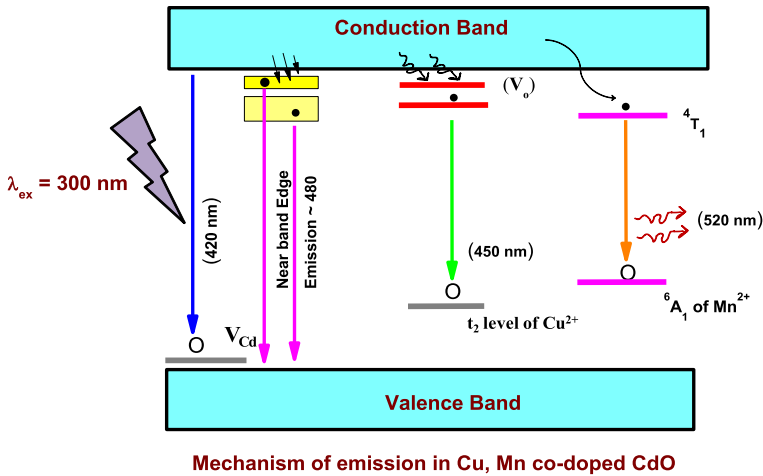
Mechanism of emission in Cu, Mn co-doped CdO

Fig. 9 Emission mechanism owing to radiative transitions in Cu^{2+}–Mn^{2+}-co-doped CdO nanocrystallites

Electrical studies

The electrical behaviors of the pellets of samples T0, T1, T2 and T3 have been carried out by the Hall measurement in Van der Pauw configuration. The overall evaluation of Cu^{2+}–Mn^{2+}-doped CdO as-prepared and annealed samples examined that all are n-type semiconductors. Detail investigation of annealing on electrical characteristics of the prepared nanopowder is executed in Fig. 10a. Table 3 represents a comparative study of different electric parameters like resistivity, mobility and carrier concentration along with band gap, conductivity and microstrain. It is observed that resistivity of the T0 sample is high (14.2 Ω m) which is diminished with annealing and acquires a minimum value of 1.4×10^{-3} Ω m for the T3 sample as shown in Fig. 10a. In fact, resistivity is dependent on the stoichiometry of the prepared Cu^{2+}–Mn^{2+}-co-doped CdO samples [6]. In this paper, PL and SEM–EDX results inferred that thermal treatment generates a non-stoichiometric composition in the prepared samples with well-ordered crystalline phase of CdO.

Moreover, carrier concentration (N) and mobility (μ_{el}) are also displayed in Fig. 10a for each sample. It is noticed that there is a significant enhancement in carrier concentration from as-prepared sample T0 (2.01×10^{19} cm^{-3}) to the highest annealed sample T3 (9.78×10^{19} cm^{-3}). This trend could be established due to the Burstein–Moss (BM) effect as observed in the prepared samples. Also, the increased crystallinity and densification at higher temperatures further improved the stoichiometry means decrement in donor type defects. However, the mobility (μ_{el}) of charge carriers is significantly enhanced in T3 as compared to T0 sample (more than 50 times). It is suggested that with annealing, the crystallite size increases due to grain boundaries shrinkage which further minimizes the scattering, and as a result, mobility of charge carriers increased. The results also resemble with other reports related to TM-doped CdO [40–43].
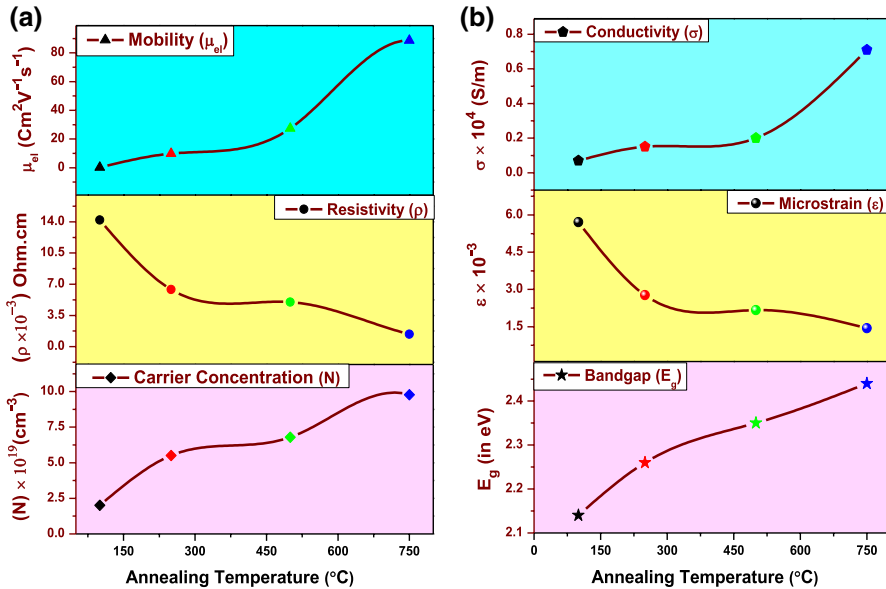
Fig. 10 **a** Variation of carrier concentration, mobility and resistivity, **b** effect of annealing on band gap, microstrain and conductivity for Cu^{2+}–Mn^{2+}-co-doped CdO nanocrystallites

Table 3 Different electric parameters of Cu^{2+}–Mn^{2+}-co-doped CdO nanocrystallites

Samples name	$\rho \times 10^{-4}$ (Ω cm)	μ_{el} (cm^2/V^1 s^1)	$N \times 10^{19}$ (cm^{-3})	Microstrain $\varepsilon \times 10^{-3}$	Conductivity $\sigma \times 10^4$ (S/m)	Band gap E_g (eV)
T0 (as-prepared)	14.2	0.24	9.78	5.71	0.07	2.14
T1 (at 250 °C)	6.4	9.82	6.79	2.77	0.15	2.26
T2 (at 500 °C)	5.0	27.39	5.51	2.17	0.20	2.35
T3 (at 750 °C)	1.4	88.64	2.01	1.44	0.71	2.44

In this study, both microstrain and band gap have played an important role to alter the electric parameters. With annealing, microstrain (ε) is decreased due to the absence of impurity phase in Cu^{2+}–Mn^{2+}-co-doped CdO nanocrystallites as shown in Fig. 10b. Band gap energy of as-prepared sample is small as compared to its bulk counterpart; however with annealing, it is slightly increased which significantly modified the carrier concentration and their mobility. Further, we have displayed the variation of conductivity in this figure which is always inversely proportional to the resistivity. Conductivity is significantly increased with temperature which resembled the mechanism of our UV–Vis spectroscopy and literature also [18]. Therefore, the obtained results of electrical study could be credited to the Cu^{2+} and Mn^{2+} ions, imperfection like oxygen vacancies, interstitial cadmium ions, microstrain and band gap variation.

Conclusions

In this report, Cu–Mn-co-doped CdO nanocrystallites were obtained by co-precipitation and a comprehensive study is performed via a suitable annealing process. XRD patterns revealed the monoclinic and hexagonal phases of Cd(OH)$_2$ in as-prepared sample which were transformed in the CdO cubic structure at 750 °C. Lattice parameters for the highest annealed sample are well matched with pure CdO means Cu^{2+} and Mn^{2+} were uniformly doped at the lattice sites of Cd ion. FTIR spectra have signature vibrations of Cd–O in the lower wave number side. SEM images emphasized that spherical nanocrystallites appeared in a brain-like morphology and successful doping of Cu^{2+}–Mn^{2+} ions confirmed by EDS spectra. In HRTEM micrographs, SAED pattern, lattice fringes, and histogram demonstrated that annealing has efficiently improved the densification and crystallinity with an average size of ~ 35 nm. Broad absorption hump appeared in the range 220–380 nm, and the band edge lies in the visible region. Band gap energy was calculated in the range 2.10–2.45 eV, and emission peaks were positioned at 420, 450, 480, 520 and 550 nm for all the samples. Annealing has generated a non-stoichiometric composition, and as a result, resistivity decreased, while carrier concentration and mobility are increased. The enhanced optoelectronic properties emphasized that the prepared nanopowder could be utilized as an alternative oxide phosphor with excellent electrical properties in nanoscale industry.

References

1. P. Sakthivel, S. Asaithambi, M. Karuppaiah, S. Sheikhfareed, R. Yuvakkumar, G. Ravi, J. Mater. Sci.: Mater. Electron. **30**, 9999 (2019)
2. T. Ghoshal, S. Kar, S.K. De, Appl. Surf. Sci. **255**, 8091 (2009)
3. A.K. Asenjun, A. Alemi, Res. Chem. Intermed. **45**, 3183 (2019)
4. N. Manjula, M. Pugalenthi, V.S. Nagarethinam, K. Usharani, A.R. Balu, Mater. Sci. Poland **33**, 774 (2015)
5. R.J. Deokate, S.V. Salunkhe, G.L. Agawane, B.S. Pawar, S.M. Pawar, K.Y. Rajpure, A.V. Moholkar, J.H. Kim, J. Alloys Compd. **496**, 357 (2010)
6. A.A. Dakhel, Mater. Chem. Phys. **130**, 398 (2011)
7. M. Thirumoorthi, J.T.J. Prakash, J. Asian Ceram. Soc. **4**, 39 (2016)
8. A.G. Imer, Superlattices Microstruct. **92**, 278 (2016)
9. S. Sivakumar, A. Venkatesan, P. Soundhirarajan, C.P. Khatiwada, Spectrochim. Acta Part A Mol. Biomol. Spectrosc. **151**, 760 (2015)
10. M. Thambidurai, N. Muthukumarasamy, A. Ranjitha, D. Velauthapillai, Superlattices Microstruct. **86**, 559 (2015)
11. B.J. Zhang, J.S. Lian, L. Zhao, Q. Jiang, Vacuum **85**, 861 (2011)
12. R. Aydin, B. Sahin, Ceram. Int. **43**, 9285 (2017)
13. R.K. Gupta, Z. Serbetci, F. Yakuphanoglu, J. Alloys Compd. **515**, 96 (2012)
14. M. Bououdina, A.A. Dakhel, J. Alloys Compd. **601**, 162 (2014)
15. A.A. Kaya, K. Erturk, Eur. Phys. J. B **92**, 121 (2019)
16. A.A. Dakhel, M.A. Khunji, A.R. Albasri, J. Electron. Mater. **47**, 4855 (2018)
17. G.T. Rao, B. Babu, R.J. Stella, V.P. Manjari, R.V.S.S.N. Ravikumar, Spectrochim. Acta Part A Mol. Biomol. Spectrosc. **139**, 86 (2015)

18. H. Çolak, O. Türkoğlu, Mater. Sci. Semicond. Process. **16**, 712 (2013)
19. S.M.H. Al-Jawad, M.M. Ismail, J. Opt. Technol. **84**, 495 (2017)
20. S. Ummartyotin, N. Bunnak, J. Juntaro, M. Sain, H. Manuspiya, Solid State Sci. **14**, 299 (2012)
21. M.I. Pratheepa, M. Lawrence, Vacuum **162**, 208 (2019)
22. C. Bhukkal, M. Chohan, R. Ahlawat, Phys. B Condens. Matt. **582**, 411973 (2020)
23. S.C. Singh, R.K. Swarnkar, R. Gopal, J. Nanopart. Res. **11**, 1831 (2009)
24. V. Eskizeybek, O. Demir, A. Avci, M. Chhowalla, J. Nanopart. Res. **13**, 4673 (2011)
25. L.A. Saghatforoush, S. Sanati, R. Mehdizadeh, M. Hasanzadeh, Superlattices Microstruct. **52**, 885 (2012)
26. C. Bhukkal, R. Ahlawat, AIP Conf. Proc. **2142**, 140017 (2019)
27. M. Khairy, H.A. Ayoub, C.E. Banks, RSC Adv. **8**, 921 (2018)
28. J.K. Rajput, T.K. Pathak, V. Kumar, L.P. Purohit, Appl. Surf. Sci. **409**, 8 (2017)
29. S. Balamurugan, A.R. Balu, K. Usharani, M. Suganya, S. Anitha, D. Prabha, S. Ilangovan, Pac. Sci. Rev. A Nat. Sci. Eng. **18**, 228 (2016)
30. K. Mohanraj, D. Balasubramanian, Silicon **10**, 1111 (2018)
31. R. Ahlawat, Ceram. Int. **41**, 7345 (2015)
32. A. Purohit, S. Chander, S.L. Patel, K.J. Rangra, M.S. Dhaka, Phys. Lett. A **381**, 1910 (2017)
33. I. Yadav, D.S. Ahlawat, R. Ahlawat, Appl. Phys. A **122**, 245 (2016)
34. K. Usharani, A.R. Balun, V.S. Nagarethinam, M. Suganya, Prog. Nat. Sci. Mater. Int. **25**, 251 (2015)
35. S. Kumar, A.K. Ojha, B. Walkenfort, J. Photochem. Photobiol. B Biol. **159**, 111 (2016)
36. R. Ahlawat, P. Aghamkar, Opt. Mater. **36**, 337 (2013)
37. N. Thovhogi, E. Park, E. Manikandan, M. Maaza, A. Gurib-Fakim, J. Alloys Compd. **655**, 314 (2016)
38. M. Benhaliliba, C.E. Benouis, A. Tiburcio-Silver, F. Yakuphanoglu, A.A. Garcíad, A. Tavira, R.R. Trujillo, Z. Mouffak, J. Lumin. **132**, 2653 (2012)
39. T. Aswani, V. Pushpa-Manjari, B. Babu, S.M. Begum, G. Rama-Sundari, K. Ravindranadh, R.V.S.S.N. Ravikumar, J. Mol. Struct. **1063**, 178 (2014)
40. F.T. Thema, P. Beukes, A. Gurib-Fakim, M. Maaza, J. Alloys Compd. **646**, 1043 (2015)
41. N. Shanmugam, B. Saravanan, R. Reagan, N. Kannadasan, K. Sathishkumar, S. Cholan, Mod. Chem. Appl. **2**, 1000124 (2014)
42. R. Kripal, A.K. Gupta, S.K. Mishra, R.K. Srivastava, A.C. Pandey, S.G. Prakash, Spectrochim. Acta Part A Mol. Biomol. Spectrosc. **76**, 523 (2010)
43. J.K. Rajput, T.K. Pathak, V. Kumar, M. Kumar, L.P. Purohit, Surf. Interfaces **6**, 11 (2017)